Analysis of Vortex Flow Phenomena on Generic Low-Aspect-Ratio Wing Configurations at Transonic Speeds

Andreas Hövelmann[1], Andreas Winkler[2], Stephan M. Hitzel[3]
Airbus Defence and Space GmbH
Rechliner Str.
85077 Manching
GERMANY

[1]Dr.-Ing, Aerodynamics Engineer, Andreas.Hoevelmann@airbus.com,
[2] Dr.-Ing, Team Leader Aerodynamic Design, Andreas.Dr.Winkler@airbus.com,
[3] Dr.-Ing, Expert Aerodynamic Design & Numerical Methods, Stephan.Hitzel@airbus.com

ABSTRACT

This article presents numerical investigations on the flow field characteristics of a generic triple-delta wing configuration at W/T size and transonic freestream conditions of Ma =0.85. The considered test case refers to another NATO-STO research task group, AVT-316, which focuses amongst others on vortex interaction effects on generic combat aircraft. The present paper extensively discusses vortex flow phenomena observed by CFD such as leading-edge vortex development, vortex-shock interactions, vortex-vortex interactions, and related vortex breakdown effects. Moreover, the flow physics analysis is set into context to selected integral force and moment coefficients. Thereby, the stability and control (S&C) characteristics are considered and assessed. The regarded angle-of-attack regime is 16° < α < 32°, discussed each for β = 0° and β = 5°. The CFD simulations originate from URANS computations with the DLR TAU-Code on unstructured hybrid grids. The results illustrate that vortex-shock interactions play a major role and considerably determine the flow field characteristics of the considered wing configuration, as they entail vortex breakdown effects or vortex-vortex interactions. Sometimes, and especially at non-zero sideslip conditions, massive changes in the flow field are observed from one angle of attack to another. Consequently, this also has a significant effect on the S&C characteristics. Pitch-up effects are commonly noticed, and a remarkable rolling-moment coefficient collapse is found at α = 22° and β = 5°. It is based on a varying vortex-shock interaction and associated upstream-moving vortex breakdown effects on the windward side of the wing, which leads to very asymmetric flow field characteristics. The corresponding asymmetric lift distribution then results in an undesired rolling-moment coefficient and the wing configuration becomes unstable in the lateral motion.

1.0 INTRODUCTION

In the view of aging fleets in Europe's air forces, a declaration of intent was made between Germany and France in 2017 to jointly work on a development of a new-generation combat aircraft [1]. In this regard, Airbus Defence and Space (Airbus DS, ADS) started various feasibility studies on generic and simplified low-aspect-ratio wing configurations, as the wide flight envelope of combat aircraft calls for suchlike wing configurations. With respect to flight physics investigations, the effort overall tends to investigate different wing planform concepts and to study related flow physical effects. The maneuverability and performance requirements of low-aspect-ratio wing configurations often result in high angle-of-attack (AoA) conditions well beyond the attached flow regime, including the presence of angle of sideslip (AoS) as well [2]. Additionally, these requirements are combined with sub-, trans- and supersonic speeds, for which significant compressibility effects are expected. The corresponding flow field characteristics are mainly dominated by leading-edge vortex flows, vortex-vortex interactions and vortex-shock interactions. In order to maintain robust and controllable stability and control (S&C) characteristics up to high AoA and AoS, the related vortex breakdown behavior is also of primary interest. This requirement adds additional challenges to the design of combat aircraft, as this type of vortex-dominated low-aspect-ratio wing configurations commonly

encounters instabilities such as pitch-up tendencies and roll reversals at medium to high AoA and AoS, often caused by (asymmetric) vortex breakdown phenomena [3]. Especially in transonic conditions, vortex-shock interactions have been found to influence the vortex breakdown behavior considerably, which complicate the flow physics phenomena and stimulate abrupt changes in the S&C characteristics [4]. In summary, the wing planform shape design and the control surfaces design thus have already a significant effect on the complexity of occurring flow physical effects, the corresponding aerodynamic coefficients, and the resulting longitudinal and lateral S&C characteristics. This includes the number of different leading edges, leading-edge sweep angles, additional strakes, the wing aspect ratio, and the sizing and layout of appropriate control surfaces. Consequently, the Airbus DS feasibility studies tend to improve the understanding of the sensitivity and effectiveness of the most driving aerodynamic shape parameters with respect to S&C and are aimed at the exploration of the relevant design space of future combat aircraft.

To widen the flow physical knowledge on suchlike low-aspect-ratio wing configurations, Airbus DS has started national cooperations with the German Aerospace Center (DLR) and the Technical University of Munich (TUM-AER). Additionally, a research task group within the NATO STO community was initiated, namely AVT-316, “Vortex Interaction Effects Relevant to Military Air Vehicle Performance” [5]. This task group has been active since 2018 and focuses amongst others on specific questions that have been arisen from the Airbus DS feasibility studies. Overall, the analyses are based on both wind tunnel (W/T) experiments and CFD simulations, and include sub-, trans- and supersonic test-case conditions. First results have already been published, especially from related experimental investigations [6-8]. On the one hand, the understanding of occurring vortex flow phenomena shall be enhanced. On the other hand, the capabilities of current CFD codes, including turbulence modeling, shall also be evaluated.

The present paper focuses on one specific test case that originates from the Airbus DS feasibility studies and was proposed to the research task group of AVT-316 (test case TC02-Com). A detailed flow physics analysis of numerical results at transonic conditions (Ma = 0.85) is presented in the following. Experimental results are not included in this article, as the focus is laid on the flow physical discussion of occurring vortex breakdown effects, vortex-shock interactions and vortex-vortex interactions. Corresponding validation results for this test case can be obtained from Reference [8]. Section 2.0 and Section 3.0 introduce the analyzed wing configuration and the applied numerical set-up for the test case, while section 4.0 then presents the corresponding CFD analysis and the detailed discussion of the results. Section 5.0 summarizes the obtained results in a synthesis and concludes on the present study and future directions. Finally, the references are given in Section 6.0.

2.0 THE GENERIC TEST-CASE MODEL ADS-NA2

The wing configuration analyzed in this paper is based on the generic low-aspect-ratio test-case model ADS-NA2 that was designed by Airbus DS. It is a 1:30-scaled version of a generic and simplified combat aircraft and is equipped with different flat-plate wing planforms including sharp leading edges and sets of corresponding control surfaces. Three different wing planforms exist in total, but here, only one particular wing configuration is regarded in its zero-control variant, namely the configuration NA2_W1_SL00, see Figure 21-1. It is characterized by a triple-delta wing planform with three different leading-edge sections. The leading-edge sweep angle of the outer main wing section is $\varphi_3 = 52.5°$, while the strake section exhibits two different leading-edge sweep angles of $\varphi_1 = 52.5°$ and $\varphi_2 = 75°$. The thickness of the flat-plate wings is d = 8 mm, including a bevel of 20° towards the sharp leading edges. Further geometric details of the wing configuration are summarized in Table 21-1. The sting of the corresponding W/T model is also considered and included in the CFD simulations, see Figure 21-1 and Section 3.0.

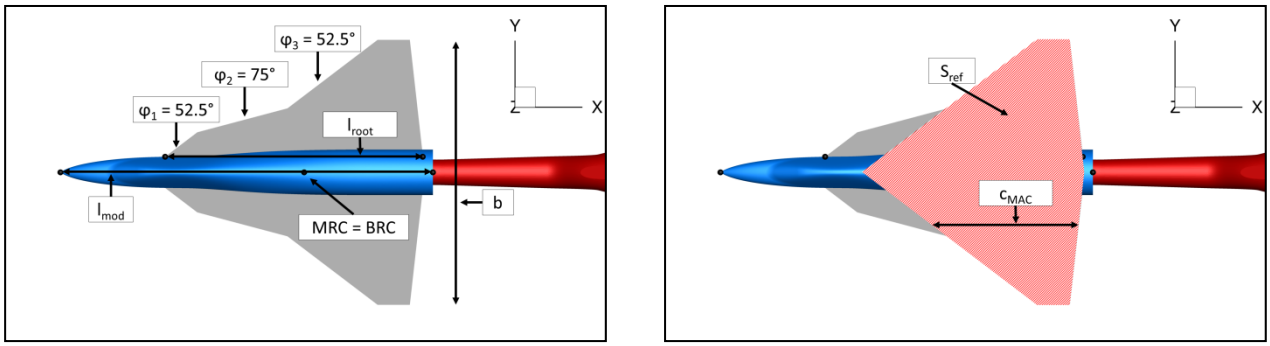

Figure 21-1: ADS-NA2 test-case model – Wing configuration NA2_W1_SL00.

Table 21-1. Geometric details of the wing configuration NA2_W1_SL00.

Model length l_{mod}	Root chord length l_{root}	Mean aerodynamic chord c_{MAC}	Wing span b	Moment reference point aft of nose x_{MRP}	Wing thickness d	Wing reference area S_{ref}
[m]	[m]	[m]	[m]	[m]	[mm]	[m^2]
0.580	0.401	0.234	0.417	0.380	8	0.082

3.0 NUMERICAL APPROACH

The CFD simulations discussed in this article were performed with the DLR TAU-Code on hybrid unstructured grids. For the mesh generation process, an in-house meshing tool of Airbus DS was applied. Based on a triangulated unstructured surface grid, the boundary layer was resolved by prismatic elements close to the boundary surfaces. In order to respect y^+ values of approximately $y^+ \approx 1$, the first prismatic cell height was set to $d_1 = 0.002$ mm and a stretching factor of f = 1.25 was applied. In total, 35 layers were used for the prism layer generation. The remaining computational volume was then filled by tetrahedral elements. In the region of the expected leading-edge vortices close to the wing surfaces, both the surface and the tetrahedral grid were considerably refined to reduce grid-induced dissipation effects. The results presented below are based on a medium-sized grid with $39.0*10^6$ nodes for the full-wing configuration. In addition, a grid resolution study was performed a priori, which led – from an industrial perspective – to a good compromise of grid size and grid convergence.

The CFD simulations were run as URANS computations with dual-time stepping approach and an implicit Backward-Euler scheme with LUSGS algorithm. The applied time step at Ma = 0.85 was set to $\Delta t = 3*10^{-5}$ s, which corresponds to a characteristic time step of $\Delta t^* = (\Delta t * U_\infty / c_{MAC}) \approx 0.04$. In total, 750 time steps were run each for the zero sideslip cases, leading to a total simulation time of $t_{sim} = 0.0225$ s. The cases with non-zero angle of sideslip were run each 3750 time steps, which corresponds to $t_{sim} = 0.1125$ s. For spatial discretization, different second-order schemes such as upwind, central with scalar dissipation and central with matrix dissipation were applied and tested. Due to higher dissipation effects induced by the upwind scheme and CFD solver stability problems with the central scheme with matrix dissipation, the following results rely on the central scheme with scalar dissipation only. The convergence behavior was additionally accelerated by well-known multigrid techniques, and a 3w cycle was used. With regard to turbulence modeling, the one-equation model SA-Neg with rotational correction was applied, which is a common standard turbulence model for industrial purposes [9-10].

The considered angle-of-attack range of the CFD simulations was $\alpha = [16°, 32°]$ with $\Delta\alpha = 1°$, and the angles of sideslip were $\beta = 0°$ and $\beta = 5°$. The freestream conditions at Ma = 0.85 were derived from the related W/T experiments, leading to a total temperature of $T_{inf,tot} = 310$ K and a total pressure of $p_{inf,tot} = 95$kPa. The corresponding Reynolds number (reference length $l_{Re} = 1$m) thus results in $Re_m = 12.53*10^6$.

4.0 RESULTS AND DISCUSSION

This section presents the results of the CFD simulations and provides a detailed flow physics analysis of the regarded test case at various angles of attack and sideslip. First, the aerodynamic coefficients are discussed for the entire angle-of-attack polars to give an overview on the overall S&C characteristics. Then, the flow physics analysis is presented for symmetric flow conditions at $\beta = 0°$ and the results are set into context to the aerodynamic coefficients. Finally, the asymmetric case with present sideslip of $\beta = 5°$ is considered.

4.1 Overview on the Aerodynamic Coefficients

Figure 21-2 depicts the aerodynamic coefficient characteristics of the NA2_W1_SL00 configuration at the test-case condition of Ma = 0.85 and $Re_m = 12.53*10^6$. The lift coefficient $C_{L,a}$ is shown in the wind-fixed aerodynamic coordinate system (index a, Figure 21-2a), the pitching- and rolling-moment coefficients $C_{m,b}$ and $C_{l,b}$ are given in the body-fixed flight-mechanical coordinate system (index b, Figure 21-2b and Figure 21-2d). In addition, the chordwise location of the aerodynamic center ($x_N - x_{LE,cMAC} / c_{MAC}$, with $x_N = dC_{m,b}/dC_{Z,b} * c_{MAC} + x_{MRP}$) is shown with respect to the mean aerodynamic chord c_{MAC} (Figure 21-2c).

The lift coefficient curve at $\beta = 0°$ indicates increasing values with increasing angle of attack up to the last AoA considered in this study, see Figure 21-2a. It seems that the maximum lift coefficient has nearly been reached at $\alpha = 32°$. The lift slope varies over the angle-of-attack polar, which is attributed to different stages of the leading-edge vortex development, vortex-shock and vortex-vortex interactions, and vortex breakdown effects, see Section 4.2. As expected, the presence of a sideslip angle ($\beta = 5°$) decreases the absolute values over the entire angle-of-attack polar. The effect becomes significant for angles of attack higher than $\alpha > 21°$, as the lift coefficient suddenly drops by 6% ($\alpha = 22°$). Then, the lift slope decreases compared to lower angles of attack, but it remains more constant with increasing angle of attack compared to the lift coefficient curve at $\beta = 0°$. At the angle of attack of $\alpha = 32°$, the lift coefficient is reduced again. Hence, the maximum lift coefficient at $\beta = 5°$ has been reached before.

The corresponding characteristics of the pitching-moment coefficient are shown in Figure 21-2b. The $C_{m,b}$ curve at $\beta = 0°$ indicates pitch-up effects for angles of attack higher than $\alpha > 20°$, for which the related derivative $C_{m\alpha,b}$ becomes positive. Then, the $C_{m,b}$ values increase non-linearly with increasing angle of attack, which reveal non-smoothly occurring flow phenomena due to vortex interactions and vortex breakdown, see Section 4.2. The pitching-moment coefficient curve at $\beta = 5°$ already shows slightly increasing values for angles of attack of $\alpha > 16°$ and results in higher values compared to the symmetric freestream case. With increasing angle of attack, the pitching-moment derivative then changes sign at $\alpha = 22°$ and the coefficient values remain nearly constant up to $\alpha = 31°$. Afterwards, the next pitch-up effect is observed. From $\alpha > 26°$ on, the $C_{m,b}$ values are lower compared to the respective curve at $\beta = 0°$.

The combined effect of both longitudinal aerodynamic coefficients can be studied in the angle-of-attack variation of the aerodynamic center, see Figure 21-2c. Additional curves are plotted for the chordwise location of the moment reference point and a fictitious design center of gravity. As the definition of the reference wing area is according to Figure 21-1 and the spanwise location of the mean aerodynamic chord is located slightly inboard of the strake wing/main wing intersection, Figure 21-2c can result in negative values as well. This then indicates that disproportionately high lift is generated in the upstream strake wing section compared to the downstream main wing section. For the angle-of-attack polar at $\beta = 0°$, pitch-up effects are observed with increasing angle of attack, as the values become negative at $\alpha = 21°$ and $\alpha = 26°/27°/28°$. Due

to the proportion of generated lift and pitching moment, the values increase again in between. At $\beta = 5°$, the curve indicates two drastic outliers at $\alpha = 21°$ and $\alpha = 32°$, where considerable changes in the flow field lead to drastic changes in the S&C characteristics. The result is consistent with the observations from the lift and pitching-moment coefficient curves, see above. In between, the variation of the aerodynamic center at $\beta = 5°$ depicts decreasing values with increasing angle of attack, thus showing pitch-up effects as well.

Figure 21-2d finally shows the rolling-moment coefficient characteristics. For the angle-of-attack polar at $\beta = 0°$, the resulting $C_{l,b}$ values are nearly zero as expected. In the presence of sideslip, however, different rolling-moment coefficient characteristics are observed with increasing angle of attack. Up to $\alpha = 21°$, the resulting $C_{l,b}$ values are negative and lie around $C_{l,b} \approx -0.01$. Consequently, the related derivative $C_{l\beta,b}$ is negative as well and stable characteristics are present. Then, however, a drastic change is observed and the rolling-moment coefficient values change to $C_{l,b} \approx +0.03$ at $\alpha = 22°$. Consequently, the leeward wing produces more lift than the windward side, the wing configuration rolls to the right and is unstable in the lateral motion. The underlying flow physics analysis to study this effect is found in Section 4.3. With increasing angle of attack, the $C_{l,b}$ values remain positive and mostly lie around $C_{l,b} \approx +0.05$. From $\alpha > 29°$ on, the values of the rolling-moment coefficient then decrease again, but still remain with positive values up to $\alpha = 32°$.

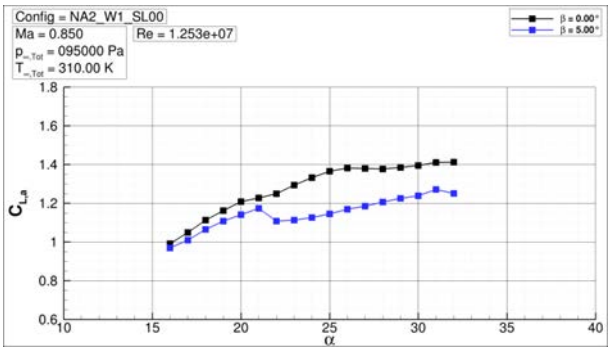

(a) Lift coefficient $C_{L,a}$.

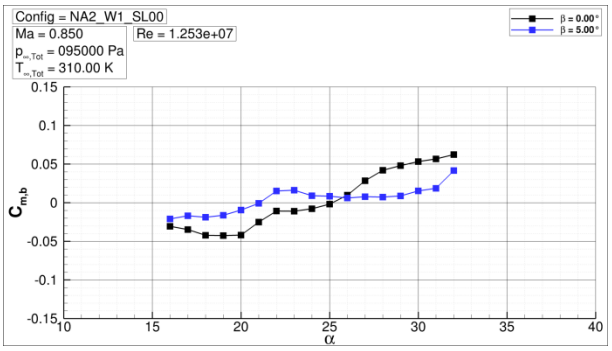

(b) Pitching-moment coefficient $C_{m,b}$.

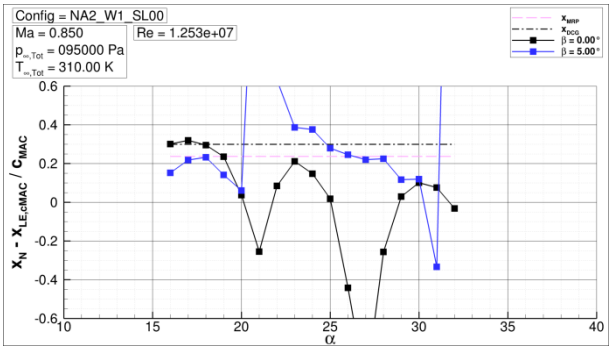

(c) Aerodynamic center $x_N - x_{LE,cMAC} / c_{MAC}$.

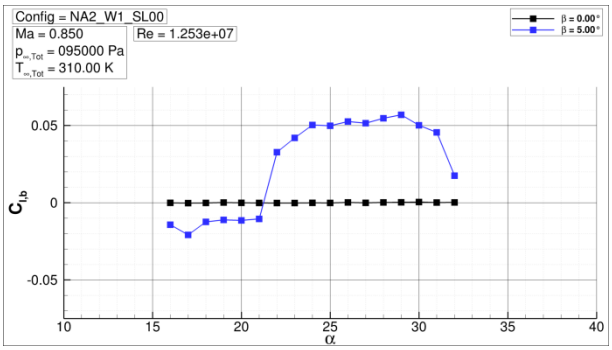

(d) Rolling-moment coefficient $C_{l,b}$

Figure 21-2: Aerodynamic coefficient characteristics of the NA2_W1_SL00 configuration versus angle of attack α.

4.2 Flow Physics Analysis at β = 0°

The corresponding flow fields of the angle-of-attack polar at $\beta = 0°$ are discussed next. For five selected angles of attack, Figure 21-3 to Figure 21-7 depict the distribution of the mean surface pressure coefficient $c_{p,mean}$ (a) and the iso surface of the non-dimensional q-criterion $Q * l_\mu^2 / U_\infty^2 = 50$ colored by total pressure loss (b). Unless it is other stated, the following discussion each refers to occurring vortices on one wing side.

At the angle of attack of α = 16°, see Figure 21-3, two decisive leading-edge vortices emerge on the triple-delta wing planform. The first one, called inboard strake vortex (ISV), originates from the strake wing section, which features two different leading-edge sweep angles. In the upstream strake wing section with φ_1 = 52.5°, the leading-edge vortex is very intense and forms a dominant suction area on the strake wing surface. At the intersection to the downstream strake wing section with φ_2 = 75°, however, a vortex-shock interaction occurs and the dominant suction area is suddenly attenuated. The shock is visible by the surface pressure increase over the entire local wing span and the center fuselage section. Vortex breakdown effects induced by the shock are not seen in this case. The areas of increased total pressure loss in the iso surface representation aft of the shock further indicate that smaller cross-flow shocks are also present in this region, see Figure 21-3b. The analysis of associated flow field cuts at constant axial positions confirm this observation (not shown). Further downstream along the strake wing, the ISV is constantly fed via the leading edge of the increased leading-edge sweep section and remains as one single leading-edge vortex. At the strake wing/main wing intersection, a second leading-edge vortex emerges and forms on the outer main wing section. It is called outboard main vortex (OMV). At approximately 60% wing span of the outer main wing, a second vortex-shock interaction occurs and terminates the suction area close to the leading edge. Again, the shock forms along the entire wing span and center fuselage section. Its position can clearly be noticed from the q-criterion iso surface and the surface pressure distribution, which shows a typical curved pattern related to transonic vortex-shock interactions [4]. The shock is seen to be the terminating shock in the downstream wing section to fulfill the flow requirements at the wing trailing edge. Thereby, vortex breakdown starts to occur for the OMV in the rear outboard wing section. For the ISV, vortex breakdown effects are not observed. Furthermore, the ISV and the OMV remain almost separated and a vortex-vortex interaction does not take place. Just in the rear wing section close to the trailing edge, the iso surface of the q-criterion indicate a beginning process of wrapping vortices.

The next angle of attack to be discussed is α = 21°, see Figure 21-4. Overall, the suction levels induced by the leading-edge vortices increase and become more dominantly. Especially in the outer main wing section, a distinct suction area originating from the OMV is observed. It is also connected to the suction contribution of the ISV, which is considerably intensified in this region. In addition, another leading-edge vortex, originating from the upstream fuselage chine (FCV), becomes present in the flow field and adds another suction contribution. Compared to α = 16°, the positions of the vortex-shock interactions move downstream. This time, the rear vortex-shock interaction can be even better seen from the surface pressure coefficient distribution, in particular for the OMV. The q-criterion iso surface of the ISV additionally results in a contraction at this position, highlighting the strength of the vortex-shock interaction. Directly aft of this shock position, the vortex-vortex interaction between the ISV and the OMV becomes more powerful, as both vortices start to interact with each other and start to wrap around. Furthermore, the process of vortex breakdown – induced by the vortex-shock and vortex-vortex interaction – is also initiated for the ISV. Altogether, this leads to the small lift slope decrease and the pitch-up effects in Figure 21-2a,b.

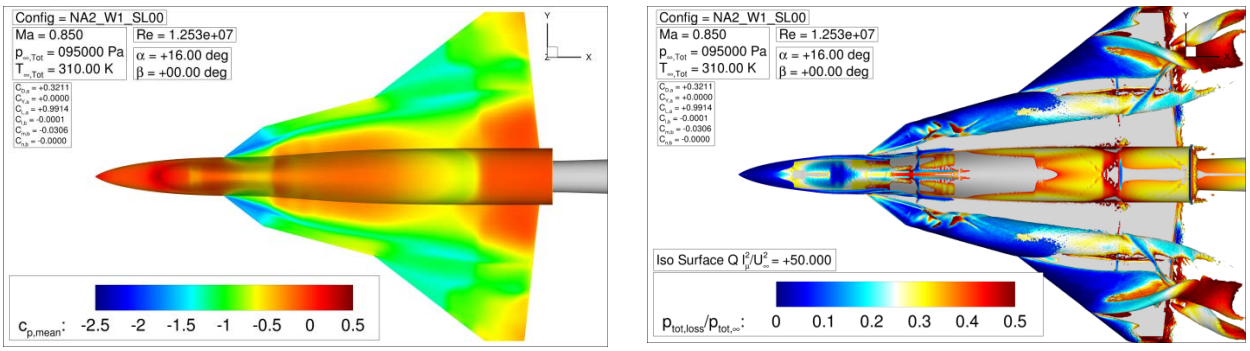

a) Distribution of means surface pressure coefficient.

(b) Iso surface of non-dimensional q criterion colored by total pressure loss.

Figure 21-3: Flow physics analysis at α = 16°, β = 0°.

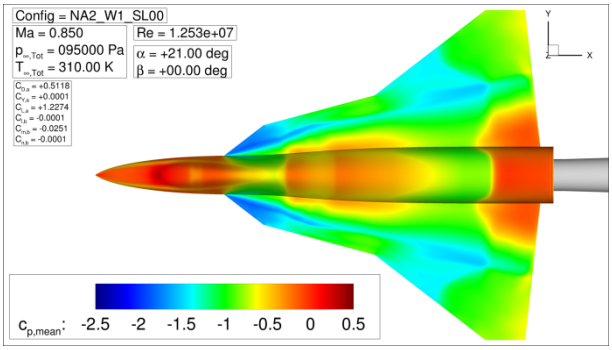

(a) Distribution of mean surface pressure coefficient.

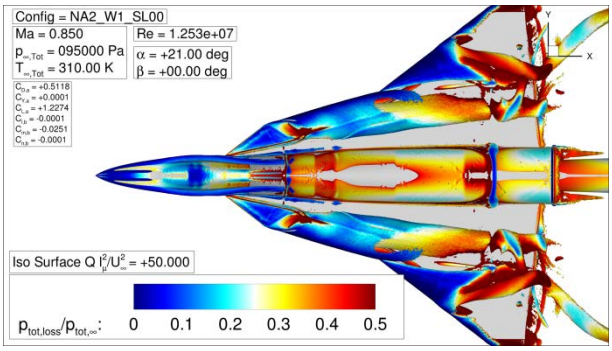

(b) Iso surface of non-dimensional q criterion colored by total pressure loss.

Figure 21-4: Flow physics analysis at α = 21°, β = 0°.

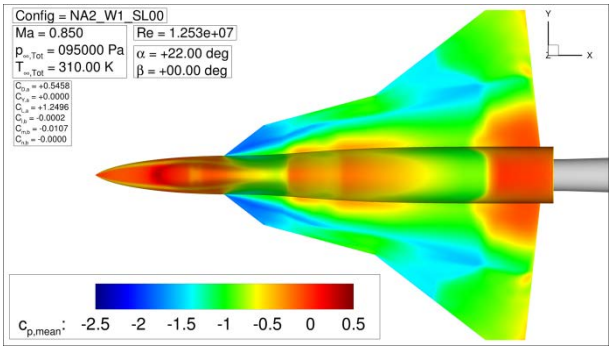

(a) Distribution of mean surface pressure coefficient.

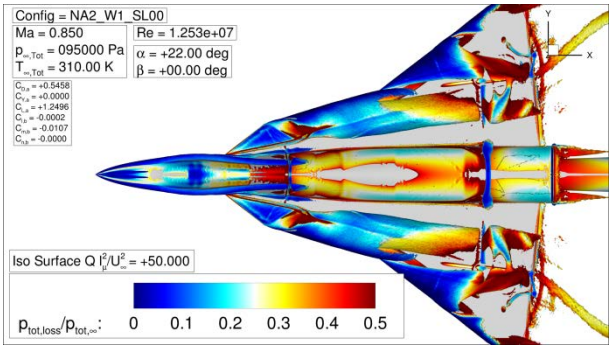

(b) Iso surface of non-dimensional q criterion colored by total pressure loss.

Figure 21-5: Flow physics analysis at α = 22°, β = 0°.

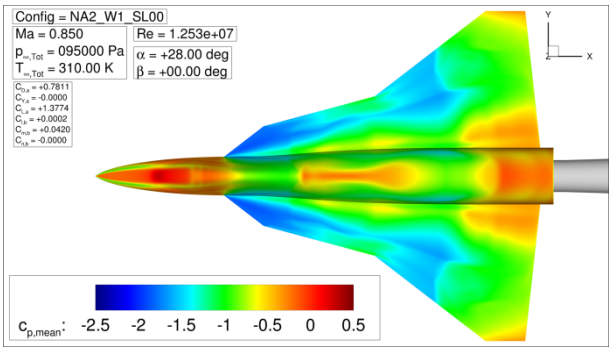

(a) Distribution of mean surface pressure coefficient.

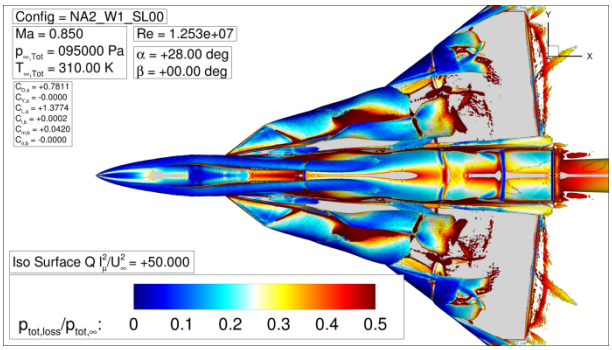

(b) Iso surface of non-dimensional q criterion colored by total pressure loss.

Figure 21-6: Flow physics analysis at α = 28°, β = 0°.

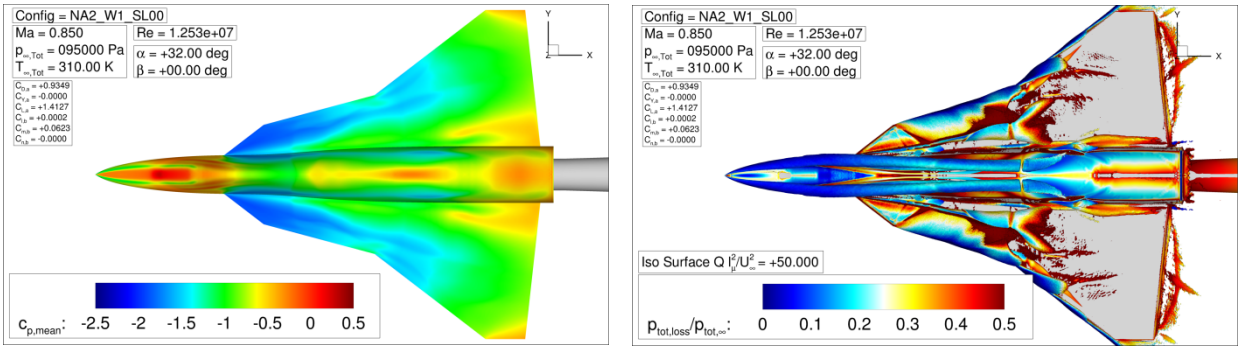

(a) Distribution of mean surface pressure coefficient.

(b) Iso surface of non-dimensional q criterion colored by total pressure loss.

Figure 21-7: Flow physics analysis at α = 32°, β = 0°.

Figure 21-5 presents the flow field results at α = 22°. While the axial position of the upstream vortex-shock interaction moves slightly downstream compared to lower angles of attack, is it shifted slightly upstream for the downstream vortex-shock interaction. This is mainly caused by the increasing strength of the ISV in the upstream strake wing section and the upstream-moving vortex breakdown of the ISV and the OMV in the downstream main wing section. Apart from that and further increased suction levels, the differences to the previously discussed angle of attack are minor, the general flow topology does not change. The shown plots mainly serve as reference for the discussion of the non-zero sideslip cases, see Section 4.3.

At the angle of attack of α = 28°, see Figure 21-6, the occurring vortex flow phenomena change. While previously, vortex breakdown was initiated by the downstream vortex-shock interaction, the upstream-moving vortex breakdown of the ISV and OMV now induce another vortex-shock interaction to the flow field around the triple-delta wing configuration. It is located at about 40% chordwise position of the outer main wing. Additionally, the induced cross-flow shocks of the ISV become more dominant and show large portions of total pressure loss in the q-criterion iso surface. Close to the strake wing /main wing intersection, this leads to vortex breakdown of the ISV, denoted by the considerable vortex core expansion. Aft of this, the additional vortex-shock interaction occurs and finally breaks up the OMV. Thereby, the strength of the terminating flow shock towards the trailing edge is reduced, which can also be seen by the attenuated surface pressure coefficient increase in the rear center fuselage section. In the strake wing section, the suction levels have increased considerably compared to lower angles of attack. The associated upstream vortex-shock interaction moves further downstream so that dominant suction areas are also noticed in the strake wing region with high leading-edge sweep. Moreover, the FCV becomes more and more powerful and its effect can both be observed in the surface pressure coefficient distribution and the q-criterion iso surface. Altogether, this generates disproportionately high lift in the upstream strake wing section and explains – together with the described vortex flow phenomena above – the increased pitch-up behaviour for angles of attack between 22° < α < 28°, see Figure 21-2.

The last angle of attack in the discussion is α = 32°, see Figure 21-7. While the suction areas in the upstream strake wing section still increase, they attenuate in the downstream main wing section due to the further propagating vortex breakdown. The associated vortex-shock interaction as first observed at α = 28° has almost reached the axial position of the strake wing/main wing intersection. Following the trend of α = 28°, the other two vortex-shock interactions become less pronounced and at least the upstream one almost disappears. The leading-edge vortex originating from the fuselage chine (FCV) is now most powerful and sinks back to the fuselage/wing surface in the downstream wing section. Its footprint can be observed in the surface pressure coefficient distribution, as the rear area of higher pressure is reduced close to the wing/fuselage intersection. It is further interesting that the FSV is not weakened by the vortex-shock interaction that is dominant at α = 32°, since the vortex core does not show any expansion afterwards.

4.3 Flow Physics Analysis at β = 5°

In this section, the flow physics analysis is presented for non-zero sideslip conditions at β = 5°. Figure 21-8 to Figure 21-12 again present the distribution of the mean surface pressure coefficient $c_{p,mean}$ (a) and the iso surface of the non-dimensional q-criterion $Q * l_\mu^2 / U_\infty^2 = 50$ colored by total pressure loss (b). The right wing side is the windward side (starboard), and the left wing side is the leeward side (port).

Due to sideslip conditions, leading-edge vortices are in general more intense but less stable on the windward side, since the effective leading-edge sweep angle is decreased. On the leeward side, they are more stable but less intense due to the increased effective leading-edge sweep angle. This behavior is already noticed at the first angle of attack to be discussed, α = 16°, see Figure 21-8. While on the windward side, the q-criterion iso surfaces of the inboard strake vortex (ISV) and outboard main vortex (OMV) are quite voluminous and end close to the trailing edge, the corresponding ones on the leeward side are more concentrated and exceed the trailing edge. Moreover, the traces of the vortex cores are shifted by the sideslip angle inboard on the windward side and outboard on the leeward side. In the associated surface pressure coefficient distribution, the suction levels are more pronounced on the windward side than on the leeward side. Apart from that, the occurring vortex flow phenomena are comparable to the zero sideslip condition and the same flow topology is present, see Figure 21-3. Two decisive vortex-shock interactions, including associated smaller cross-flow shocks in the ISV, occur in the flow field around the triple-delta wing configuration. A beginning vortex-vortex interaction is noticed close to the trailing edge on the leeward side. Otherwise, both the ISVs and the OMVs remain separated at α = 16° and β = 5°.

At the angle of attack of α = 21°, see Figure 21-9, the resulting flow field becomes more asymmetric on the wind- and leeward side of the wing. In particular, this is seen by the downstream vortex-shock interaction, which is rotated upstream on the windward side and downstream on the leeward side. Starboard, the vortex-shock interaction involves massive vortex breakdown effects, and the abrupt increase of the surface pressure coefficient in the outer main wing section has already propagated significantly upstream towards the strake wing/main wing intersection. On the port side, the vortices are still unperturbed by the flow shock and do not show any vortex breakdown. In contrast, the ISV and OMV interact with each other to a greater extent close to the trailing edge. The asymmetric surface pressure distribution is also observed in the upstream strake wing section, in which the suction levels are more pronounced and elongated on the windward side. This is accompanied by more intense cross-flow shocks that evolve further downstream in the ISV. Altogether, the vortex flow phenomena lead to different integral values of the lift coefficient on the starboard and port wing. The rolling-moment coefficient, see Figure 21-2d and the text box in Figure 21-9b, is negative, which is consistent with the described flow field observations. The lift contribution of the windward side is greater than that of the leeward side so that the configuration would roll to the left. Hence, stable characteristics are present, which is desired and would convert the sideslip angle to an increased angle of attack.

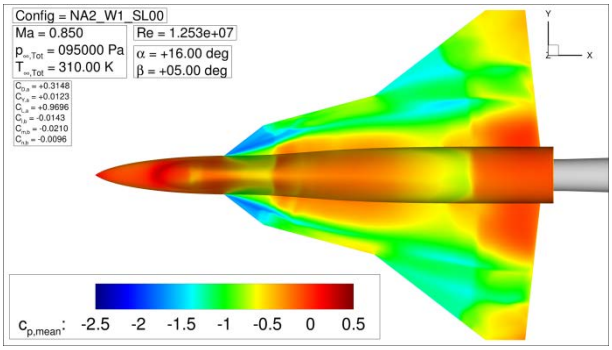

(a) Distribution of mean surface pressure coefficient.

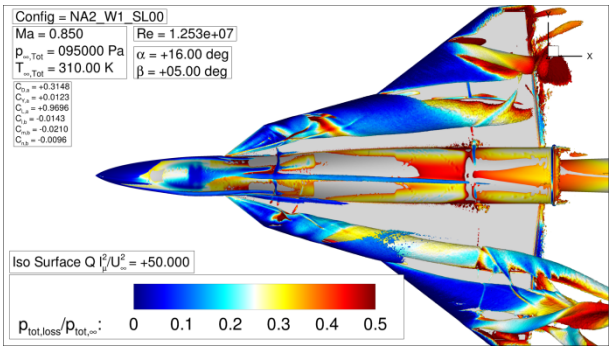

(b) Iso surface of non-dimensional q criterion colored by total pressure loss.

Figure 21-8: Flow physics analysis at α = 16°, β = 5°.

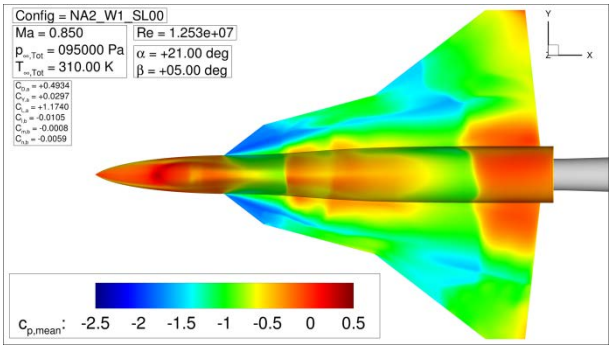

(a) Distribution of mean surface pressure coefficient.

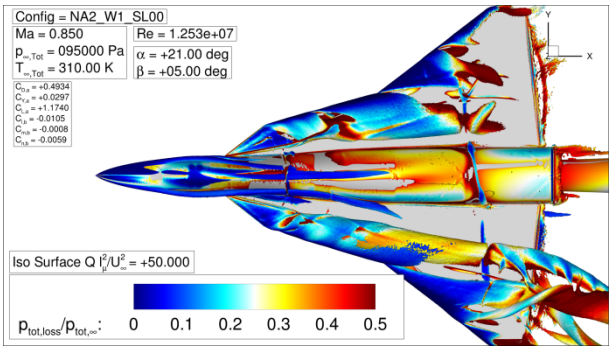

(b) Iso surface of non-dimensional q criterion colored by total pressure loss.

Figure 21-9: Flow physics analysis at α = 21°, β = 5°.

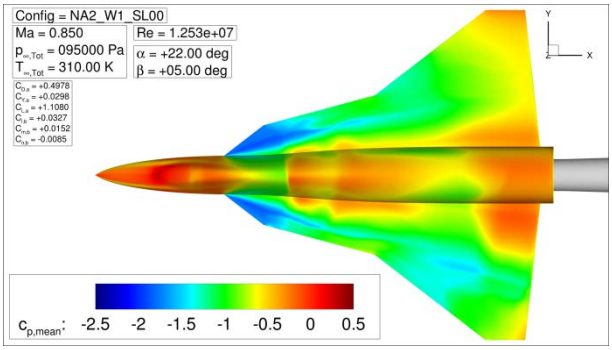

(a) Distribution of mean surface pressure coefficient.

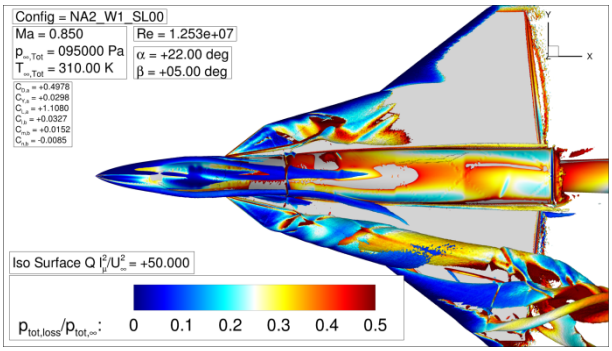

(b) Iso surface of non-dimensional q criterion colored by total pressure loss.

Figure 21-10: Flow physics analysis at α = 22°, β = 5°.

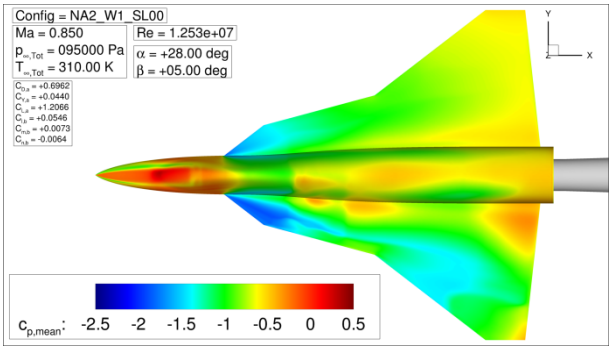

- (a) Distribution of mean surface pressure coefficient.

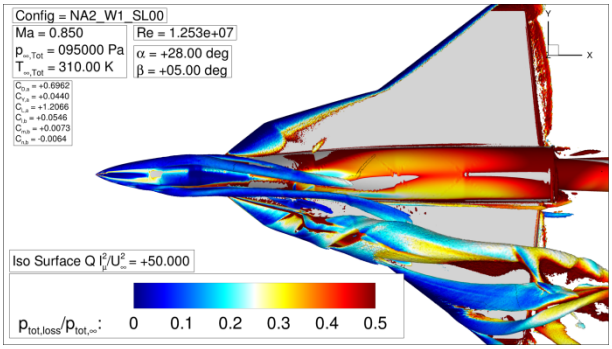

(b) Iso surface of non-dimensional q criterion colored by total pressure loss.

Figure 21-11: Flow physics analysis at α = 28°, β = 5°.

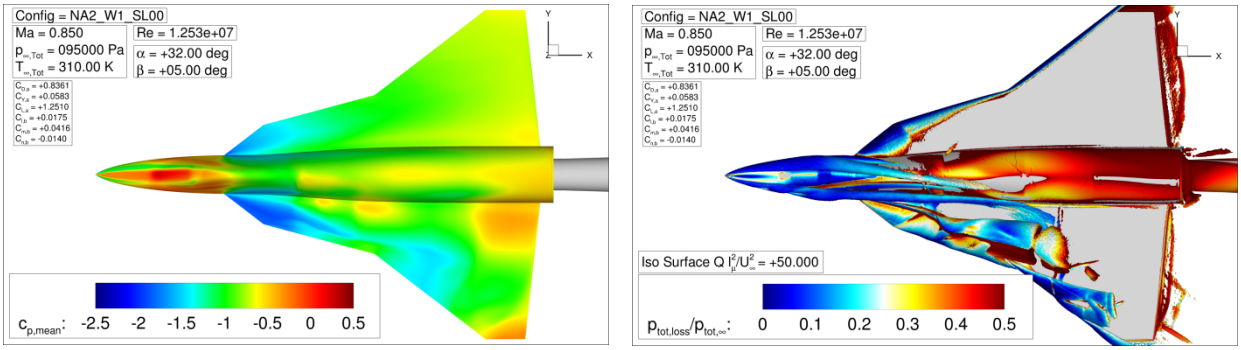

- **(a) Distribution of mean surface pressure coefficient.**

(b) Iso surface of non-dimensional q criterion colored by total pressure loss.

Figure 21-12: Flow physics analysis at α = 32°, β = 5°.

The next angle of attack to be discussed is α = 22°, see Figure 21-10. In comparison to the previous described plots at α = 21°, the flow field has changed significantly, especially on the windward side. The downstream vortex-shock interaction is not visible anymore and the starboard surface pressure coefficient distribution is altered considerably. Vortex breakdown of the ISV suddenly jumps upstream of the strake wing/main wing intersection, the OMV is instantly burst close to the main wing leading edge, and the corresponding suction levels on the main wing surface decrease significantly. Based on the chosen value of the q-criterion, the OMV is not depicted any longer by the iso surface. Consequently, generated lift in the rear wing section is lost and the lift distribution is changed towards the upstream strake wing section. There, the suction levels induced by the ISV are also influenced by the upstream-propagated vortex breakdown, but they still increase on a moderate level. These observations are in line with the integral values of the lift and pitching-moment coefficients, see Figure 21-2a-c. On the leeward side, the rear vortex-shock interaction is still present as it can be seen from the $c_{p,mean}$ values close to the wing/fuselage intersection and the curved pattern of the surface pressure coefficient in the left main wing section. The strength of the shock has decreased and both the port ISV and the OMV are still not weakened so that they do not show vortex breakdown tendencies. The vortex-vortex interaction close to the trailing edge becomes more dominant and moves slightly upstream. Since additionally the upstream suction region associated with the ISV becomes more powerful, it turns out that the port wing now produces more lift than the starboard wing. Consequently, the rolling-moment coefficient must change sign, as it is seen in Figure 21-2d. Within one degree angle-of-attack increase, the present triple-delta wing configuration thus shows a massive collapse in the rolling-moment coefficient, which leads to unstable lateral S&C characteristics.

Figure 21-11 depicts the flow field results at α = 28° and β = 5°. The plots indicate that on the windward side, vortex breakdown of the ISV has propagated upstream on the strake wing section, which leads to reduced suction levels close to the strake wing leading edge. Further downstream, the surface pressure distribution alters to a region with relatively constant values, which is attributed to the dead water region of the burst ISV and OMV. On the leeward side, the ISV becomes more intense in the upstream strake wing section as it is expected. In line with the observations for the zero sideslip case, the upstream vortex-shock interaction moves downstream and is attenuated. The downstream vortex-shock interaction also reduces in strength and is not as dominant as before. It is interesting to note that both fuselage chine vortices (FCV) now reach the left wing and contribute thereby to stable vortex characteristics on the leeward side. It seems that the left FCV and the ISV start to interact with each other so that the vortex trace of the ISV is shifted inboard. Thereby, the associated vortex-vortex interaction between the port ISV and OMV is slightly shifted downstream. In summary, the generated lift difference between both wing sides is intensified at α = 28° and β = 5°. For this reason, the associated rolling-moment coefficient rises to $C_{l,b} \approx +0.05$, see Figure 21-2d. In terms of the integral lift coefficient on the entire triple-delta wing configuration, however, is turns out that

the dead water region still contributes to an increase of the global $C_{L,a}$ value. The associated pitching-moment coefficient is on the same level compared to $\alpha = 22°$ and no further pitch-up is observed, which is consistent with the collapse of the ISV in the strake wing section.

The last angle of attack in the discussion with sideslip conditions is $\alpha = 32°$, see Figure 21-12. The relative change of the surface pressure coefficient distribution on the windward side is rather small. The uniformity of the moderate suction levels on the main wing surface is slightly increased and the dominant region of low surface pressure close to the strake wing leading edge is not diminished any longer. On the leeward side, in contrast, this time the flow field changes considerably. The stable coexistence of the port ISV and OMV is no longer present. Instead, the ISV exhibits a remarkable vortex breakdown close to the axial position of the strake wing/main wing intersection. It comes along with an obvious vortex core expansion. Thereby, the suction levels in the rear main wing section are reduced. It is worth to state that the vortex breakdown location is close to the position where the left FCV interacts with the port ISV. The rear vortex-shock interaction of the OMV is still present at $\alpha = 32°$, but it is observable only from the surface pressure coefficient distribution. It can be noticed that the axial position has moved upstream and the strength is increased, as the pressure increase is more abrupt than at $\alpha = 28°$. For this reason, the q-criterion iso surface can capture the OMV to a lesser extent than before. Having understood the flow field changes at the present angle of attack, it becomes clear why the associated rolling-moment coefficient starts to decrease again, see Figure 21-2d. Due to the collapse of the leeward ISV/OMV vortex system and its transformation to a dead water region as it is already present on the windward side, the flow field characteristics become less asymmetric and the undesired lift difference between right and left wing is reduced. Consequently, the $C_{l,b}$ values reduce and tend to reach negative values again at higher angle of attack. Moreover, the pitch-up effect as indicated in Figure 21-2b is thereby also explained.

5.0 SYNTHESIS AND CONCLUSION

Complex vortex flow phenomena occurring on a generic low-aspect-ratio wing configuration at transonic speeds have been presented and discussed in this article. The analyzed geometry and test-case condition refer to the currently-running NATO-STO research task group AVT-316, which deals with “Vortex Interaction Effects Relevant to Military Air Vehicle Performance”. In general, the activity is aimed at a better understanding of vortex flow effects in sub-, trans- and supersonic test-case conditions for triple- and double-delta wing planforms, which are known to show specific challenges in the S&C characteristics with increasing angle of attack and sideslip angle. The wing geometries analyzed in AVT-316 are generic and simplified fighter-type flat-plate wing configurations, which were designed at Airbus Defence and Space.

The results presented in this paper originate exclusively from CFD simulations on the NA2_W1_SL00 wing configuration and are based on URANS computations with the one-equation turbulence model SA-Neg with rotational correction (RC). Experimental results exist for this particular wing configuration and the considered test-case condition at Ma = 0.85, and they have been published before [8]. For the current article, however, the focus has only been set to a detailed description of the flow field characteristics observed by CFD and the related discussion on selected integral force and moment coefficient values. Thereby, the analyzed flow field phenomena could be set into context to the resulting S&C characteristics. Due to the considered transonic freestream conditions, vortex-shock interactions occur in the flow field around the triple-delta wing configuration and are, additionally to vortex-vortex interactions and vortex breakdown effects, relevant for the resulting S&C behavior. Compared to subsonic vortex flow field investigations, which are commonly analyzed in this field of study, this adds another complexity and has not been often discussed before.

The present flow physics analysis at $\beta = 0°$ and at $\beta = 5°$ has shown complex vortex flow phenomena that emerge on the triple-delta wing configuration with increasing angle of attack. Two dominant leading-edge vortices (inboard strake vortex and outboard main vortex, ISV and OMV) occur from different leading-edge

sections and start to interact with each other. At high angles of attack, additional fuselage chine vortices (FCV) come into play as well. Vortex-shock interactions are commonly present in the corresponding flow fields and determine the characteristics of the leading-edge vortices. Depending on local flow field conditions and vortex development stages, sometimes vortices have been found to be unperturbed by occurring vortex-shock interactions. In other situations, the results point out that the vortex-shock interactions have a significant impact on following vortex breakdown effects or vortex-vortex interactions. These phenomena therewith determine considerably the suction levels on the wing surface and consequently the generated lift distribution. In conjunction with non-zero sideslip conditions, asymmetric flow fields have been observed, which partially undergo massive changes from one angle of attack to another. As a result, the longitudinal and lateral moment coefficients $C_{m,b}$ and $C_{l,b}$ are highly affected with increasing angle of attack.

At zero sideslip conditions with $\beta = 0°$, the NA2_W1_SL00 configuration shows pitch-up effects due to vortex-shock interactions and associated vortex breakdown effects for angles of attack of $\alpha > 20°$. The related lift coefficient characteristics are also influenced. At non-zero sideslip conditions with $\beta = 5°$, pitch-up tendencies are already present for angles of attack of $\alpha > 16°$. Between $\alpha = 21°$ and $\alpha = 22°$, the flow field changes remarkably so that the global S&C characteristics are significantly influenced. Due to very asymmetric flow field characteristics on the windward and leeward side of the wing configuration, the pitch-up effect is stopped for the present, the lift coefficient drops by 6%, and a massive rolling-moment coefficient collapse with $C_{l,b}$ values changing from $C_{l,b} \approx -0.01$ to $C_{l,b} \approx +0.03$ is observed. Consequently, the wing configuration is not stable in the lateral motion any longer and tends to roll to the right. The asymmetric flow field characteristics are mainly attributed to different vortex-shock and vortex-vortex interactions as well as vortex breakdown effects on the windward and leeward wing side, respectively, which occur based on the different effective leading-edge sweep angles. These characteristics remain rather similar up to $\alpha = 31°$, before the vortical structures on the leeward side massively break up at $\alpha = 32°$ as well so that the asymmetry is reduced. As a result, the rolling-moment coefficient is reduced again, but another pitch-up is observed.

The available results including the presented flow physics analysis point out how complex vortex flow characteristics can become in transonic freestream conditions for even such a simplified and generic wing configuration. In the view of the design of new-generation combat aircraft, for which increased requirements are also present to the aerodynamic design, the understanding of associated flow field characteristics and the resulting S&C behavior is thus essential. The transonic regime plays in this context a decisive role, as robust and controllable S&C characteristics are hardly to reach but contribute to a large extent to agility and maneuverability of fighter-type aircraft. The present article has given some explanations to induced vortex flow phenomena on suchlike low-aspect-ratio wing configurations and to their effect on stability and control. Some questions regarding the occurrence of vortex-shock interactions are still under discussion, especially when they occur together with vortex breakdown effects. Often it is hard to judge whether a vortex-shock interaction provokes vortex breakdown effects or vice versa. If this dependency and the corresponding cause-and-effect relation is better understood, suchlike vortex flow phenomena can also be used as design tool for desired flow field characteristics. In particular, this holds for the design and use of favorable wing planforms as well as sophisticated control surfaces on combat aircraft wing configurations, which can provoke or prevent the development of new leading-edge vortices, can influence vortex-shock or vortex-vortex interactions, or which can regulate the occurrence and characteristics of vortex breakdown effects. This then would further give an added value to the aerodynamic design and development of future combat aircraft.

6.0 REFERENCES

[1] Factsheet Future Combat Air System - Anteil Next Generation Weapon System – NGWS, data available online at https://www.bmvg.de/resource/blob/24288/6548107ac4b24da5611745b18252099a/20180427-factsheet-future-combat-air-system-anteil-next-generation-weapon-system-data.pdf, retrieved June 2019

[2] Hitzel, S.M. ; "Flight Physical Aspects and Methods of Future Military Aircraft Designs" ; 63rd Deutscher Luft- und Raumfahrtkongress, Augsburg, Germany, September 16-18, 2014

[3] Hitzel, S.M. ; "Combat Aircraft Vortex Flow Challenges – Separation, Interaction and Breakdown" ; NATO-STO Specialists Meeting on "Progress and Challenges in Validation Testing for Computational Fluid Dynamics", Avila, Spain, September 26-28, 2016, No. 21 in MP-AVT-246

[4] Schiavetta, L. , Boelens, O. , Crippa, S. , Cummings, R.M. , Fritz, W. , Badcock, K.J. ; "Chapter 29 – Shock Effects on Delta Wing Vortex Breakdown"; NATO-STO Technical Report AVT-113 on "Understanding and Modeling Vortical Flows to Improve the Technology Readiness Level for Military Aircraft", NATO-STO, Neuilly-sur-Seine Cedex, France, October 2009

[5] NATO-STO AVT-316 description, data available online at https://www.sto.nato.int/Lists/test1/activitydetails.aspx?ID=16476, retrieved June 2019

[6] Hitzel, S.M. , Winkler, A. , Hövelmann, A. ; "Vortex Flow Aerodynamic Challenges in the Design Space for Future Fighter Aircraft" ; STAB Symposium 2018, Darmstadt, Germany, November 6-7, 2018

[7] Pfnür, S. , Pflüger, J. , Breitsamter, C. ; "Analysis of Vortex Flow Phenomena on Generic Delta Wing Planforms at Subsonic Speeds" ; STAB Symposium 2018, Darmstadt, Germany, November 6-7, 2018

[8] Hövelmann, A. , Winkler, A. , Hitzel, S.M. , Richter, K. , Werner, M. ; "Analysis of Vortex Flow Phenomena on Generic Delta Wing Planforms at Transonic Speeds" ; STAB Symposium 2018, Darmstadt, Germany, November 6-7, 2018

[9] Spalart, P.R. , Allmaras, S.R. ; "A One-Equation Turbulence Model for Aerodynamic Flows" ; 30th AIAA Aerospace Sciences Meeting & Exhibit, Reno (NV), United States, January 6-9, 1992; No.439 in AIAA 1992

[10] Allmaras, S. R., Johnson, F. T., and Spalart, P. R.; "Modifications and Clarifications for the Implementation of the Spalart-Allmaras Turbulence Model"; 7th International Conference on Computational Fluid Dynamics (ICCFD7), Big Island (HI), United States, July 9–13, 2012.